POLITECNICO DI TORINO
Repository ISTITUZIONALE

Non-Reactive Experimental Analysis of an Exhaust Section downstream of a CVC

Original
Non-Reactive Experimental Analysis of an Exhaust Section downstream of a CVC / Gallis, P., Misul, D.A., Boust, B., Bellenoue, M., Salvadori, S.. - ELETTRONICO. - (2025), pp. 1-14. (European Turbomachinery Conference (ETC16) Hannover, Germany March 24-28, 2025).

Availability:
This version is available at: 11583/2999064 since: 2025-04-22T10:02:09Z

Publisher:
European Turbomachinery Society

Published
DOI:

Terms of use:

This article is made available under terms and conditions as specified in the corresponding bibliographic description in the repository

Publisher copyright

(Article begins on next page)

25 November 2026

Proceedings of the 16th European Turbomachinery Conference (ETC16)
Turbomachinery, Fluid Dynamics and Thermodynamics,
March 24-28, 2025; Hannover, Germany

Non-Reactive Experimental Analysis of an Exhaust Section downstream of a CVC

Panagiotis Gallis[1], Daniela Anna Misul *[1], Bastien Boust[2], Marc Bellenoue[2], and Simone Salvadori[1]

[1]Department of Energy, Politecnico di Torino, Corso Duca degli Abruzzi 24 10129, Torino, Italy
[2]Pprime Institute, CNRS-ENSMA-University of Poitiers, Avenue Clèment Ader 1 86961, Chasseneuil, France

Abstract

The overall architecture of gas turbines has been recently re-evaluated by investigating innovative cycles aimed at substantially increasing the thermal efficiency. One attractive solution is the pressure gain combustion cycle and in particular the Constant Volume Combustor (CVC) technology. The aim of this paper is to present the experimental results obtained analyzing an exhaust system designed to integrate a CVC with a high-pressure turbine vane. In particular, the geometry of the CVC tested at the PPrime Institute has been considered for the design of the new device. That CVC uses a mixture of air and liquid iso-octane, while an isochoric, exothermic process is ensured by using two pairs of rotary valves. The newly-designed transition duct aims at greatly reducing the flow fluctuations generated by the valves, and is positioned between the CVC and an existing converging-diverging nozzle. Two windows are placed at the top and at the side of the duct to allow for performing particle image velocimetry analysis. The current experimental campaign is inert as fuel injection does not take place. Two different test runs have been performed by varying the inlet stagnation pressure of the combustion chamber. Obtained results demonstrate the ability of the duct to both accelerate the flow field and reduce the time-dependent distortions generated by the exhaust valves. The presented results also pave the way for a following reactive campaign, which is expected to prove the overall concept and to provide fundamental information about the coupling between the CVC and the turbine.

Keywords: Combustor-Turbine Interaction, Particle Image Velocimetry, Pressure Gain Combustion, Constant Volume Combustion

1 Introduction

The Pressure Gain Combustion (PGC) technology was initially introduced by Holzwarth [1], who suggested to exploit the concept of isochoric combustion inside of Gas Turbine (GT) cycles. The fundamental difference between the Brayton and PGC cycles relies in the fact that in the latter case the stagnation pressure of the burnt gases increases during the combustion process [2], thus reaching a higher theoretical thermal efficiency value [3] and reducing the specific fuels consumption if compared with conventional cycles, both in the propulsion and the power generation fields [4].

Component interaction has always been one of the most relevant topics in GT design and operation [5]. Usually, vanes and blades are designed based on the assumption of steady inflow conditions, whereas PGC cycles are characterized by pulsating combustor outlet flows. Therefore, increasing attention has been paid to the study of the integration of PGC modules with turbine stages to quantify the effect of a pulsating inflow condition on turbine efficiency. Fernelius *et al.* [6] experimentally evidenced the reduction of the efficiency of an axial turbine working under a low-frequency axial flow pulsation. It was also demonstrated that the fluctuation of the incidence angle plays a major role in performance degradation. Pioneering recommendations for the design process of turbine airfoils that work under pulsating conditions were provided based on experimental data [7, 8]. More problems arise in the case of Pulsed Detonation Engines (PDE) [9] and Rotating Detonation Engines (RDE) [10, 11], which are characterized by the occurrence of detonation processes along with the combustion process. In fact, the beneficial effect on the cycle efficiency associated with the pressure increase occurring in the combustion chamber is limited by the development of a pulsating outflow that is characterized by a supersonic Mach number, which may be responsible for the un-starting of the cascade that is positioned downstream of the Rotating Detonation Combustor (RDC) [12]. To cope with that limitation, Liu *et al.* [13, 14] designed a High-Pressure Turbine (HPT) vane characterized by diffusive end-walls, which ensured the ingestion of the high-enthalpy flow coming from the RDC. Moreover, the HPT vane and the end-walls have been optimized to attenuate the total pressure fluctuations and maximize the efficiency [15–17]. In addition, cooling holes positioned in the diffusive part of the end-walls have been successfully exploited as passive flow control systems aimed at reducing secondary flows intensity [18].

A relevant experimental contribution to the RDC/HPT interaction set of studies has been provided by Naples *et al.* [19], who replaced the combustion core of the T63 (C20–250) gas turbine with an RDC. They demonstrated that the turbine efficiency is weakly affected by the pulsation of the flow thanks to its high passing frequency (usually around 10 kHz) and to the inertia of the flow, that does not react to incoming solicitations with a comparable frequency. The presence of a rotating oblique shock also plays a major role in the effective integration of a RDC into a HPT stage [20]. It was proved that if the oblique shock is not aligned with the stagger angle of the vanes, a complex wave reflection system occurs [21] and total pressure attenuation through the cascade happens [22]. In fact,

*Corresponding author: daniela.misul@polito.it, tel. +39 0110904436

an experimental study done by Bach *et al.* [23] demonstrated that higher performance can be obtained when the stagger angle is aligned with the oblique shock since this configuration generated a lower amount of reflecting shocks, thus facilitating the starting of the vane passages. Subject of the analysis was the NACA 0006 airfoil. In the case of PDEs, Glaser *et al.* [24] integrated experimentally a series of can-annular Pulsating Detonation Combustors (PDCs) with a HPT stage [24]. In that case it was concluded that the sequential firing of PDC tubes was the main reason of the reduced turbine performance.

In addition to the RDC technology, which is based on supersonic detonation, the Constant Volume Combustion (CVC) technology allows for increasing the total pressure of the mixture across the combustion process by means of subsonic deflagration. The CVC process is conceptually similar to the one occurring in internal combustion engines. In gas turbines, it generates a pulsating flow characterized by high enthalpy and very high turbulence levels that oscillates without shocks and with limited tangential non-uniformities at the module exit section. Therefore, it is very challenging to perform detailed measurements at the exhaust of a CVC in order to investigate the complex outflow for the integration with a HPT stage.

The current paper presents the results obtained through an experimental campaign aimed at analyzing the flow field development in a newly-designed CVC exhaust section, and is supported by the EU-funded Marie Sklodowska-Curie Action INSPIRE. The prototype machine selected for the current research has been designed and tested at the PPrime Institute [25] and consists of a chamber with a pair of inlet and outlet rotary valves. First, fresh air is guided inside of the chamber. Then, direct injection of liquid iso-octane takes place and a spark-plug igniter is used to trigger the combustion with closed valves. The combustion process can be considered isochoric and the total quantities of the medium significantly rise after the exothermic process. Finally, the valves open and the burnt gases are expanded at atmospheric conditions. The exhaust system consists of a rectangular plenum mounted to a circular converging-diverging nozzle. An extensive parametric experimental campaign performed by varying the operating frequency, the exhaust plenum sizes, and the nozzle throat diameter provided valuable results for the operation of the CVC rig [26]. It was concluded that both the local spark timing velocity and the residual burned gases characteristics are crucial parameters for the combustion process, as it was numerically confirmed by Large Eddy Simulations [27].

Efforts were made to investigate how the CVC can be integrated with a HPT stage. First, a 1D model tuned to reproduce the experimental data of the test rig was created, focusing on the specification of the transient conditions downstream of the exhaust valves [28–30]. Then, an unsteady numerical optimization procedure allowed for designing a transition duct able to attenuate the pulsating outflow of the CVC before reaching a HPT vane [31]. The unsteady numerical analysis of the ensemble exhaust system of the CVC, which consisted of the plenum, the transition duct and the vane, demonstrated that newly-designed exhaust system guarantees 10.6 % of total pressure attenuation over 2.96 % of stagnation pressure losses.

The transition duct designed by Gallis [31] *et al.* is then modified to serve the needs of the experimental test rig operated at the PPrime Institute. Downstream of it, a circular converging-diverging nozzle is mounted to mimic the backpressure effect of the HPT vane. At this first stage of the analysis, neither injection nor ignition occur inside of the chamber, thus neglecting the effects of the combustion process. However, the fast rotation of the valves is preserved generating perturbations of total pressure inside of the duct. These flow oscillations are the subject of this study. The instrumentation of the activity includes three fast response pressure measurements located inside of the chamber, both upstream of the transition duct and downstream of it. In addition, low frequency Particle Image Velocimetry (PIV) analysis is conducted at the meridional section of the transition duct. Two levels of inlet stagnation pressure of the test rig are tested, namely 2 *bar* and 4 *bar*. The transient acceleration inside the connective component is captured and thoroughly described for different moments of the cycle. This study allows for both describing the complex aerodynamic behavior of the coupled CVC/duct system and demonstrating the capability of the new device to weaken the flow oscillations. It is also a fundamental step towards the upcoming analysis of the reactive case, which paves the way for a highly detailed experimental investigation of the unsteady outflow from a CVC by using reactive PIV.

2 Experimental Apparatus

In this section, the experimental rig and the instrumentation of the test section are discussed. In particular, the test rig is presented in Section 2.1. A detailed description of each part and the functional purpose of every component is provided. Section 2.2 focuses on the measurement techniques that are used in this study. First, the pressure measurements are presented, then the PIV analysis of the perturbing exhaust flow field follows. In the end, Section 2.3 describes the potential uncertainty sources of the study.

2.1 Test Rig

The experimental test rig is displayed in Fig. 1a. The system starts with the intake tank (1), which supplies air at a temperature $\approx 14\ ^oC$ to the system. The stagnation pressure of the air can be modified by a pressure dome regulator [26] positioned upstream of the intake plenum. Afterwards, there is the inlet plenum (2), that leads the air inside of the combustion chamber (3). The combustion chamber has a pair of inlet and outlet rotary valves. Fresh air enters inside of the chamber when the inlet valves are open and the exhaust valves are closed. Then, the inlet valves close and direct injection of liquid iso-octane occurs inside of the chamber. With the help of a spark plug igniter an isochoric combustion takes place as both inlet and outlet rotary valves are closed. Afterwards, only the exhaust valves of the chamber open thus allowing the combustion products to expand through the exhaust section to atmospheric conditions. Finally, both inlet and outlet valves open, the chamber is supplied with fresh air and the cyclic operation of the CVC keeps repeating. The outtake system of the CVC consists of a rectangular exhaust plenum (4) and of the

newly designed device (5). An isometric visualization of the exhaust system is reported in Fig. 1b, where the laser source for the PIV (6) and the camera (7) are visible. Moreover, the cut-view reported in Fig. 1c shows that the exhaust system is divided into a transition duct (i), a change area duct (ii) and a converging-diverging nozzle (iii) that flows out at atmospheric conditions.

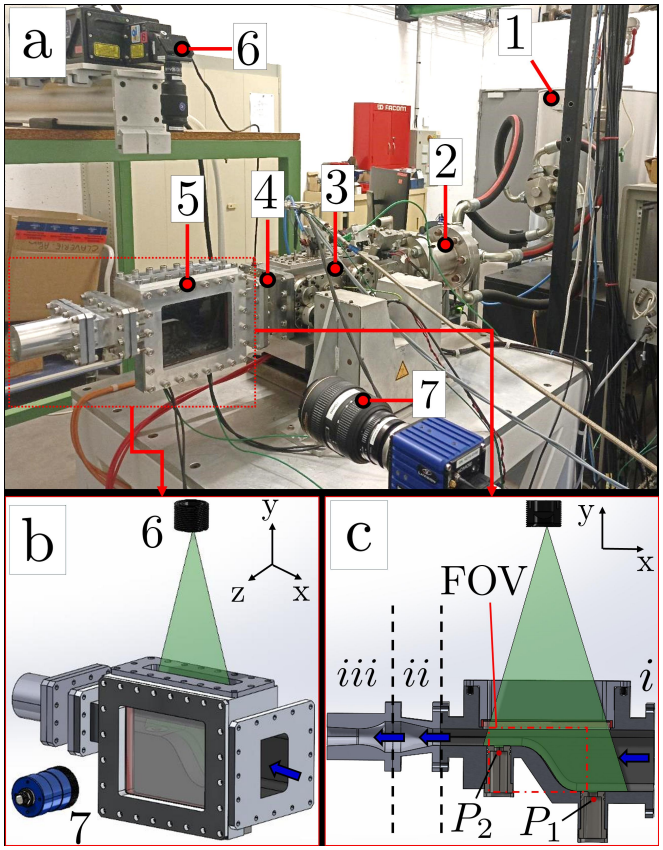


Figure 1: Experimental Test Rig (a), Isometric View of the Exhaust System (b) and Cut-View of the Exhaust System (c).

The geometry of the duct used in this experimental activity (referred to as "Man", manufactured) differs from the one originally designed by Gallis *et al.* [31] (referred to as "Opt", optimized). The meridional profile of the Opt transition duct is reported in Fig. 2a and is the result of a numerical activity which had as a goal the integration of the CVC exhaust with a HPT vane [31]. The optimization process allowed for designing a meridional profile that alleviated the time-dependent fluctuation of the exhaust flow field. However, the profile of the Man transition duct reported in Fig. 2a is quite different. In fact, due to the PIV measurements requirements it is necessary to have a flat window in the upper part of the exhaust wall. For that reason, the manufactured transition duct of Fig. 2a keeps the same area ratio of the optimized case (see Fig. 2b), but with a flat upper end-wall.

Also, the Opt transition duct was designed to connect the exhaust plenum of the CVC with the LS89 annular cascade [32]. The cascade is omitted from the experimental campaign and a duct with a variable area distribution (referred to as (ii) in Fig. 1c) is used to transform the rectangular section to a circular one and connect it with a converging-diverging nozzle (referred to as (iii) in Fig. 1c). The geometrical features of the nozzle are the same as of the previously performed experimental analysis [26]. Its design is based on the ISO-9300 norm [33] with a throat diameter of 20 *mm*, which corresponds to an area that is equivalent to the one of the LS89 annular cascade used for the optimization by Gallis *et al.* [31].

Finally, the present experimental case is inert while the Opt geometry was obtained considering a reactive case and the hot exhaust gases from the CVC. The combustion process is not included in this analysis that aims at studying the aerodynamics of the Man device, which are not known from previously performed numerical activity. However, the CVC cyclic rotation of the inlet and exhaust valves is maintained as well as the filling-emptying process of the chamber. As a result, highly oscillating airflow passes the exhaust section due to the fast valves rotation.

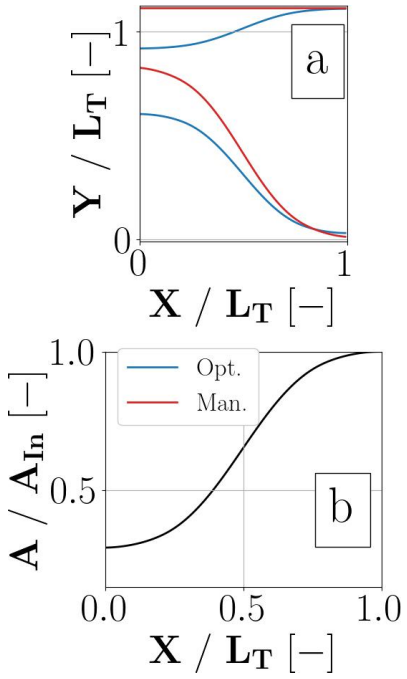


Figure 2: Comparison of Optimized and Manufactured Transition Duct Profiles (a) and Area Ratio Evolution (b).

In this experimental work two cases are investigated, in which the incoming air has total pressure of 2 *bar* and 4 *bar* resulting in test rig pressure ratio (Eq. 1) of 0.51 and 0.25 respectively. Since the outflow of the CVC is significantly pulsating, the outlet velocity is not constant. As a result, a reference Reynolds number is used for the two cases, in accordance with Equation 2. In this expression, the speed of sound of the medium at the upstream tank (1 in Fig. 1a) of the test rig is computed. As characteristic length is used the length of the transition duct L_T. Moreover, the effective cycle of the valves is set to 25 Hz for both cases. In Table 1, the characteristic numbers of the two experimental sets are enlisted.

$$\pi_{rig} = \frac{P_{atm}}{P_{t,\,in}} \tag{1}$$

$$Re_{rig} = \frac{\mu \rho V}{L_{char.}} \rightarrow Re_{rig} = \frac{\mu_{T_{t,\,in}} (\frac{P_{t,\,in}}{RT_{t,\,in}}) (\sqrt{\gamma R T_{t,\,in}})}{L_T} \qquad (2)$$

Case	$\mathbf{P_{t,\,in}}$	$\mathbf{T_{t,\,in}}$	$\mathbf{f_{cycle}}$	$\pi_{\mathbf{rig}}$	$\mathbf{Re_{rig}}$
a	2 *bar*	14 ^oC	25 Hz	0.51	$3.2 \cdot 10^6$
b	4 *bar*	14 ^oC	25 Hz	0.25	$6.47 \cdot 10^6$

Table 1: Conditions of Two Experimental Sets.

2.2 Measurement Equipment

The instrumentation of the test rig includes fast response pressure measurements and PIV analysis. Concerning the pressure measurements, three sensors are employed in this study whose sampling frequency is 100 kHz. A Kistler 4011 recessed sensor is implemented inside of the combustion chamber. The goal of this sensor is to monitor the pressure fluctuations upstream of the exhaust section. Afterwards, the focus of the analysis is on the newly-manufactured exhaust section. Two sensors locations P_1 and P_2 can be seen in Fig. 1c. A Kistler 4007 recessed sensor is placed upstream of the transition duct, while a Kistler 4049 flush-mounted sensor is positioned downstream. These two sensors track the pressure values upstream and downstream of the accelerating region. Overall, these three sensors help providing the magnitude of the pressure fluctuations upstream of the exhaust valves, upstream of the transition duct, and downstream of it. Also, the static pressure measurement at P_1 location can state whether the downstream nozzle is choked or not. In fact, due to the low velocity at the P_1 location, which is positioned before the geometrical restriction of the transition duct, it can be assumed that the static pressure level is very close to the stagnation pressure downstream of the exhaust valves.

Concerning the PIV analysis, the laser source (6) and the camera (7) can be identified in Fig. 1a and Fig. 1b. The low frequency PIV system uses Quantel Evergreen to generate a laser sheet of $2 \cdot 100$ mJ/pulse at 25 Hz. The Imager sCMOS camera with a resolution of 2560×2160 pixels of $6.5\ \mu m \times 6.5\ \mu m$ size captures the oscillating outflow. Silicon oil droplets are used for the seeding purposes. In fact, seeding takes place at the intake plenum (1 in Fig. 1a). In Fig. 1b, the two glass windows are displayed. The upper window ensures the penetration of the laser sheet, while the lateral window allows for optical access inside of the transition duct. In Fig. 1c, the Field of View (FOV) is presented. The goal of the PIV is to analyze the transient acceleration of the exhaust flow through the transition duct. In addition, it can be highlighted that the laser sheet scans the middle of the transition duct including P_1 and P_2 sensors. Moreover, the Programmable Timing Unit (PTU X) coordinates the synchronization between the laser sheet and the camera. After the end of the experiments, the DaVis commercial software [34] is used for the post-processing of images. An interrogation window 16×16 pixels with 25 % overlap is applied.

The rotational speed of the pair of both inlet and outlet valves is set at 750 rpm (12.5 Hz). Nevertheless, during one rotation, the valves open and close twice. As a result, the effective frequency of the cycle is 25 Hz (40 ms). In Fig. 3, the valves lift law is illustrated. The blue dashed curve describes the lift law of inlet valves (In-Valve), while the red dashed curve (Ex-Valve) shows the lift law of the exhaust valves for one full valve rotational period. Since the experimental activity is non-reactive, the cycle variability between two consecutive cycles is negligible. For every different moment of the cycle, the exhaust flow field in the transition duct is expected to be almost identical from cycle to cycle. Thus, it is allowed to be performed ensemble averaging technique on the PIV measurements.

The aforementioned frequency of the PIV system is 25 Hz. Consequently, a single PIV sample is allowed per cycle. Therefore, a repetitive process is needed to capture the evolution of a periodic exhaust field. The CVC test rig operates in total for 200 cycles (8 s). Therefore, each cycle is split into 20 segments of constant time step of 2 ms. The 20 different time delays of the PIV process are illustrated with dashed vertical lines in Fig. 3. As a result, for every of the 20 time splits of the cycle, 200 PIV samples occur. By averaging for each of the 20 time delays the 200 PIV samples, the ensemble averaging of the cycle is achieved. For example, the experimental test rig operates for 200 cycles and the PIV system monitors the exhaust field at 25 Hz with a time delay of 25 % of the cycle. As a result, 200 different PIV fields for the first time delay of 25 % are sampled at the end of the experimental test. By averaging these 200 different PIV events, the ensemble average PIV field for the 25 % of the cycle is accomplished. Similarly, an experimental test is performed again for 200 cycles, but the PIV time delay is set to 30 % of the cycle. In the end, the ensemble average PIV field of 30 % of the cycle is performed by averaging the new 200 different PIV fields. By proceeding repetitively to the remaining 18 time delays, the ensemble average PIV field for 20 different cycle moments is reconstructed. In total, 20 different experimental tests are performed for each case. Thus, 4000 PIV samples are recorded for each case of Table 1.

2.3 Uncertainty of Measurements

The fast-response sensors used for the pressure measurements are piezoresistive. The uncertainty level specified by the manufactured (Kistler) is at 0.2 % of the measurement value. In parallel, it is important to investigate the uncertainty sources of the PIV measurements in order to define the level of accuracy of the study. In PIV analysis, uncertainties arise mainly due to system components (e.g. installation and alignment, timing and synchronization, particle tracing capabilities, illumination), due to the flow, and due to the evaluation techniques [35]. The uncertainty quantification can been seen in Equation 3. In fact, the uncertainty of velocity vector (δv) is split into the uncertainty due to the particle displacement ($(\delta v)_{\Delta X}$), due to laser pulse separation ($(\delta v)_{\Delta t}$) and due to magnification ($(\delta v)_M$). The error arose by the temporal difference of the two laser emission (Δt_l) is usually in the order of 1 ns. The analysis utilizes Δt_l in much higher order of magnitude ($[7-15]\ \mu s$). Therefore, this type of uncertainty can be

considered negligible. In parallel, the contribution of uncertainty due to the magnification can be considered almost zero as well, since the magnification field is considerably larger than the dimensions of micro-fluid applications.

$$\delta v = (\delta v)_{\Delta X} + (\delta v)_{\Delta t} + (\delta v)_{M} \tag{3}$$

As a result, the uncertainty originated by particle displacement can solely characterize the uncertainty of the velocity vector measurements. Hence, let us consider a defined vector field grid, and j a specific location of this grid. For every time moment of the cycle t, the ensemble average velocity vector ($\tilde{v}_j(t)$) is derived by averaging a certain number of time instances (N_{EA}) of this specific vector (Eq. 4). For the current experimental campaign, the N_{EA} is equal to 200. Similarly for the same grid location, the standard deviation of the recorded vectors that constitute the ensemble average vector can be computed (Eq. 5). As a consequence, the uncertainty of the ensemble average velocity vector v at the specific location of the grid j for the every time moment of the cycle t is given by Equation 6 [34].

$$\tilde{v}_j(t) = \frac{1}{N_{EA}} \sum_{i=1}^{N_{EA}} \tilde{v}_{i,j}(t) \tag{4}$$

$$\sigma[\tilde{v}_j(t)] = \sqrt{\frac{1}{N_{EA}} \sum_{i=1}^{N_{EA}} [v_{i,j}(t) - \tilde{v}_j(t)]^2} \tag{5}$$

$$\delta v_j(t) = \sigma[\tilde{v}_j(t)] \sqrt{\frac{1}{N_{EA}}} \tag{6}$$

By sequentially performing these computations on every grid point j, the uncertainty velocity vector profile can be specified for every time moment of the cycle t. The ensemble averaging process offers 20 different velocity profiles, consequently 20 different uncertainty velocity profiles as well. A useful statistical evaluation can be the cycle assessment of this property. As a result, for every grid point j, the cycle average uncertainty of the velocity vector v for a period T is given by Equation 7. In accordance, the standard deviation of the uncertainty during the cycle can be computed by Equation 8.

$$\hat{\delta v_j} = \frac{1}{T} \int_0^T \delta v_j(t)\, dt \tag{7}$$

$$\sigma(\delta v_j) = \sqrt{\frac{1}{T} \int_0^T [\delta v_j(t) - \hat{\delta v_j}]^2\, dt} \tag{8}$$

Hence, after the post-processing of the velocity vector profiles it is possible to retrieve the cycle average and cycle standard deviation behavior of the velocity vector uncertainty profile. In particular, there are two sources that generate significant uncertainty levels in the flow field. First, the oil used for lubrication purposes of the valves passes through the exhaust system and is accumulated close to the upper straight end-wall of the duct. Similarly, accumulation of lubricating oil can occur at the start of the lower end-wall contouring of the transition duct. As a result, when the laser scans these location, excessive illumination can happen imposing difficulties on the cross-correlation of those zones. In parallel, on both upper and lower end-walls, fillet radius is used at the right side of the transition duct's entrance, as it can be seen in Fig. 1b. This fillet modification propagates along the transition duct's length. These curved parts of the transition duct are absent by the PIV field, as the laser sheet scans the FOV at the middle cross-section of the transition duct (see Fig. 1c). Nevertheless, parasitic reflections may arise from these zones, which are in the background of the analyzed flow field, interfering with the resulting vector field.

3 Experimental Results

The results of the experimental campaign are presented in Section 3. In Section 3.1 the pressure traces at the chamber, upstream and downstream of the transition duct for the two cases are discussed. The results of the PIV analysis are included in Section 3.2, then a performance comparison between the two cases takes place in Section 3.3.

3.1 Pressure Measurements

In Fig. 3, the evolution of static pressure both upstream and downstream of the transition duct is reported for case *a* and case *b* (see Table 1). The signals of these three sensors are derived after applying a Phase-Locked Averaging (PLA) analysis utilizing the rotation period of the valves (80 *ms*) instead of the cycle (40 *ms*) period. However, due to the lack of combustion, the dynamics inside of the chamber and in the transition duct do not change during every cycle. Thus, the PLA signals of $0-40$ *ms* ($[0-1]$ of t/T_{cycle} in Fig. 3) are identical with the time window of $0-80$ *ms* ($[1-2]$ of t/T_{cycle} in Fig. 3) for the three sensors for both inlet conditions.

Starting from the first case of Fig. 3a, when both valves are closed the chamber is highly pressurized, while the locations of the transition duct approaches the atmospheric pressure. The gaps of inlet and outlet valves allow a very small portion of leaking air for exiting the chamber and expanding inside of the transition duct. As the exhaust valves open ($0-30$ % of cycle), the pressure inside of the chamber drops, while an increase of pressure level is observed for the P_1 and P_2 sensors. In fact, the chamber pressure level approaches the one of the transition duct at the 30 % of cycle. Later, the intake valves open ($30-55$ % of cycle), while the exhaust valves remain open as well. The penetration of air inside of the chamber significantly increases the pressure inside of it. Similarly, the pressure upstream and downstream of the transition duct increases. The transition duct pressure value reaches its maximum at 50 % of cycle, as the exhaust valves are about to close (55 % of cycle). As the outtake valves are closed ($55-70$ % of cycle), the effect of the opening of the inlet valves is evident only to the chamber, in which the pressure is still increasing. On the contrary, a constant decay is observed for the pressure sensors of the transition duct. When the intake valves close at 70 % of cycle, the chamber pressure maintains a high level, while a negligible decay is observed due to the leakage of the exhaust valves. On the other hand, the air in the exhaust system is still being discharged to atmospheric conditions. After 85 % of the cycle, the pressure levels across the transition

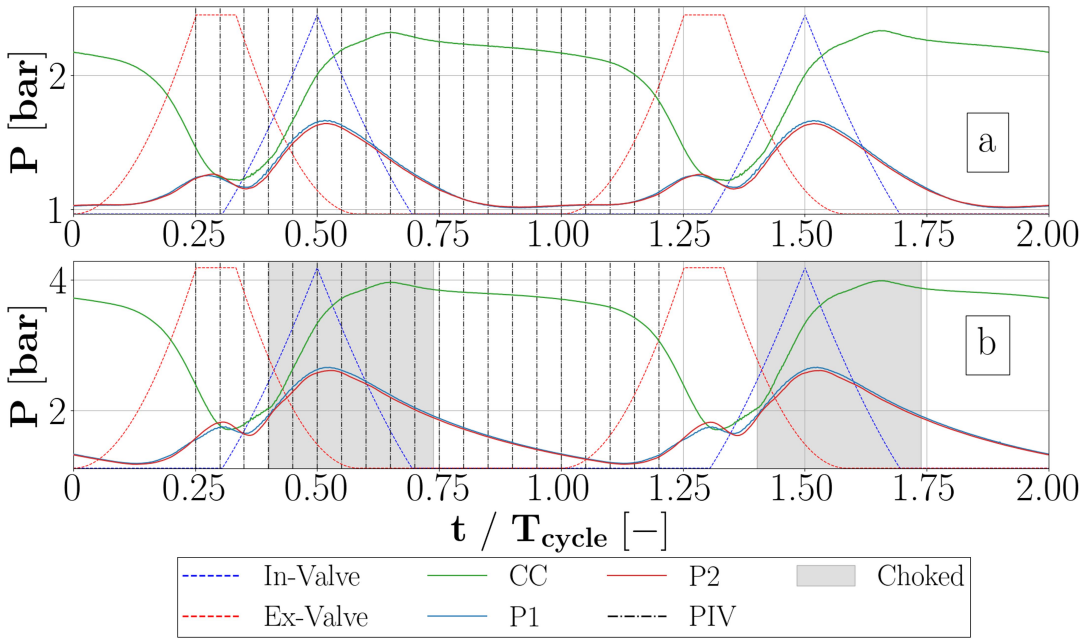


Figure 3: PLA Pressure Traces at Combustion Chamber, Upstream and Downstream of Exhaust System for Case *a* & *b*.

duct approach the atmospheric value by expanding the leakage flow from the chamber though the exhaust valves. An identical repeated cycle can be observed for the next periodic time frame of $100-200$ % of the cycle.

Likewise, the pressure traces for the case *b* are displayed in Fig. 3b. There are four main differences between the two cases. First, the level of pressure for all the sensors is obviously higher for the second case. In fact, the higher stagnation pressure in the supply system of the test rig increases the level of static pressure of all the components. A second difference can be observed in the morphology of the decay of transition duct sensors. In Fig. 3b, P_1 and P_2 do not reach the atmospheric pressure during the common valves closing time window ($70-100$ %), as happened in case *a*. On the contrary, a constant decay is observed. This difference is explained by the fact that there is still air inside the exhaust system that needs to be discharged. For the case *a*, the majority of the air in the exhaust system is already expanded before of the common closing valves time window. Thus, the level of pressure approaches the atmospheric value and the exhaust system expands the leakage flow by the exhaust valves. On the contrary, in the case *b* the common closing valves time window is not wide enough to completely empty the exhaust system.

Later, a misleading conclusion can be derived, since the chamber pressure exceeds the supplying stagnation pressure (2 *bar*) in Fig. 3a. Nonetheless, the significant dynamics inside of the chamber due to the opening and closing of inlet and outlet exhaust valves oscillate the pressure. Hence, perhaps the amplitude of the oscillation surpasses the stagnation pressure, but in average the pressure inside of chamber is lower than the inlet supplying total pressure. However, in Fig. 3b the chamber's pressure do not exceed the inlet total pressure. For the two different cases, the different pressure ratios (Table 1) lead to different oscillating massflow rates and total pressure losses. Thus, it is necessary to characterize the oscillation of pressure for the three sensors. The time-average pressure value (Eq. 9) and the standard deviation (Eq. 10) of pressure signals derived by the PLA of Fig. 3 are normalized with the help of inlet total pressure for the two cases respectively. The results can be seen in Table 2. The elevated inlet supplying pressure and the further reduced test rig pressure ratio of case *b* induces more losses in the inlet supply system providing the chamber with less pressure comparing to case *a*. In addition, the transition duct is able to reduce the standard deviation of the pressure from inlet (sensor 1) to outlet (sensor 2) for a cycle for both cases.

$$\hat{P} = \frac{\frac{1}{T}\int_0^T P\,dt}{P_{t,\,in}} \tag{9}$$

$$\sigma(\hat{P}) = \frac{\sigma(P)}{P_{t,\,in}} \tag{10}$$

Case	Sensor	$\hat{\mathbf{P}}$	$\sigma(\hat{\mathbf{P}})$
a	cc	98.39 %	17.98 %
	1	61.1 %	10.29 %
	2	60.73 %	9.83 %
b	cc	82.31 %	18.08 %
	1	44.58 %	11.35 %
	2	44.09 %	11.05 %

Table 2: Statistical Analysis of PLA Pressure Evolution of Case *a* and *b*.

The fourth difference lies on the performance of the exhaust nozzle. As already mentioned, it can be assumed that the pressure trace of P_1 is quite close to the total pressure trace due to the low Mach number value of the flow. Thus, this sensor gives a reliable estimation of the stagnation pressure upstream of the exhaust nozzle. As it is evident, the estimated stagna-

tion pressure of the exhaust nozzle varies in time. Considering that the gas is expanded to the atmospheric pressure, the pressure ratio of the exhaust nozzle varies as well (Eq. 11). Since no heat addition or work extraction occurs in the test rig, the temperature of the medium can be considered constant. In addition, no combustion takes place and the composition of gas is kept the same. As a result, the specific heat capacity ratio (γ) of the medium is unaltered, and the constant critical pressure ratio of the exhaust nozzle is given by Equation 12. Since the varying pressure ratio of the exhaust nozzle is known, the moments of the cycle in which the nozzle is choked can be specified. Based on the obtained data, it is concluded that the low level of supplied pressure of case *a* is not enough to bring the pressure ratio of the nozzle below the critical. On the contrary, in case *b* the nozzle is choked during ≈ 34 % of the cycle. The latter case is close to the time window of the reactive case (≈ 50 % of cycle) found by a numerical study of Gallis *et al.* [29].

$$\pi_{Nozzle} = \frac{P_{atm}}{P_{t,\,1}} \approx \frac{P_{atm}}{P_1} \tag{11}$$

$$\pi_{cr} = \left(\frac{\gamma+1}{2}\right)^{\frac{-\gamma}{\gamma-1}} \tag{12}$$

3.2 PIV Measurements

PIV analysis is able to shed light on the phenomena occurring in the transition duct. In Fig. 4, PIV flow fields in the exhaust system are portrayed for the time moments $25-50$ % of the cycle for the case *a*. These time instances are selected as they provide the most interesting information about the flow field inside of the transition duct. In fact, it is the time window in which the exhaust valves are open and the intake valves start to open as well. The analysis finishes just before the closing time of the exhaust valves. A similar representation of the varying exhaust flow field of the transition duct for the exact same cycle moments for case *b* can be found in Fig. 5.

At 25 % of cycle for case *a*, the exhaust valves are completely open, while the intake valves are closed. The effect of the exhaust valves can be observed in the inlet of the FOV, where a vortex is generated inside of the plenum by the expansion of the flow. The flow crosses the valves and generates a vortex that is placed upstream of the transition duct and partially of the FOV as well. The concentrated white "cloud" on velocity field implies the presence of a vortex. In particular, this structure is a counterclockwise vortex. On the next time step (30 % of cycle), the vortex can be seen moving towards the down wall at the start of the transition duct. At 35 % of cycle, it can be detected in a lower position and closer to the start of the transition duct. At 40 % of the cycle, the vortex is pushed towards the initial part of the lower wall of the transition duct and starts to decrease its intensity due to the opening of the inlet valves. The effect of intake system is evident after 40 % of the cycle, when the static pressure of the transition duct sensors rises. When the exhaust valves are ready to close ($45-50$ % of cycle), the effect of the exhaust valves is no more visible as the vortex disappears. Also, there is no indication of a newly-generated vortex and the inlet velocity profile is quite uniform. It can be here reported that the velocity field inside the transition duct remains uniform in the $55-100$ % of cycle interval. As the valves are closed no effect is noticed. Although, a constant deceleration of the flow field is observed till the moment of the opening of the exhaust valves (100 % of cycle). Afterwards, the transition duct experiences an acceleration till the 120 % of cycle, when the cycle repeats again.

Similarly, the analysis can be extended for the same time moments for case *b* in Fig. 5. A first conclusion is that the transition duct accelerates more the outflow with respect to case *a*. A vortex can be identified again at 25 % of cycle. Conversely to case *a*, the vortex has a clockwise rotation. At the next time step, the vortex enters inside of the FOV, while a great acceleration can be detected in the middle lower end-wall of the transition duct. The vortex recedes at 35 % of cycle, while in the next moment the effect of the inlet valves is visible. The vortex is pushed downstream towards the upper wall of the transition duct, while the maximum outlet velocity speed is achieved ($\approx 130\ m/s$). As the exhaust valves close, the vortex is located at the start of the upper wall, while its size is decreased. At 45 % of cycle, it is entirely inside the FOV. Later, the velocity field is more uniform and a constant deceleration is observed after the closing of the exhaust valves ($55-100$ % of cycle). With the opening of the outlet valves (100 % of cycle), the flow field inside of the transition duct is accelerated till the 120 % of period. Later, a new cycle starts again.

The two cases exhibit two different types of vortices with two different trajectories. The sudden expansion by the exhaust valves opening ($25-40$ % of cycle) generates a vortex which only its half is firstly evident, while its subsequent trajectory uncovers all its entity. The reason why the two cases exhibit different sign of rotation of this vortex cannot be directly answered. First of all, the exhaust valves constitute three equal time-varying flow cross section in vertical direction ($y-$ axis) [29]. Nonetheless, downstream of the exhaust valves the area restriction of the transition duct is not equally distributed (see Fig.2a $y-$ axis). The restriction occurs only to the upper part of the duct. Thus, the pressure distribution at the entrance of the transition duct is not expected to be uniform at the vertical direction ($y-$ axis). Consequently, the three equal time-varying flow cross sections of the exhaust valves do not experience the same pressure gradient. Therefore, they provide the exhaust plenum and subsequently the transition duct with different massflow rates. This imbalance of pressure gradient for two cases generates different sign of rotation. Nonetheless, the reasons for clockwise or counterclockwise rotation would potentially be uncovered either through similar experimental visualizations, including the upstream portion of the plenum, or with advanced transient CFD analysis, including the valve bodies.

In Fig. 6a, the cycle average uncertainty velocity vector profile of the case *a* is portrayed, while the standard deviation is seen in Fig. 6b. It is evident that the lubricating oil deposition at upper end-wall ($y/L_{FOV} > 0.6$) significantly increases the level of uncertainty. Moreover, the background curved walls close to the exit of the transition duct ($x/L_{FOV} \in [-1,-0.6],\ y/L_{FOV} \in [0.52,0.6]$) generate parasitic reflections increasing the error of velocity measurements.

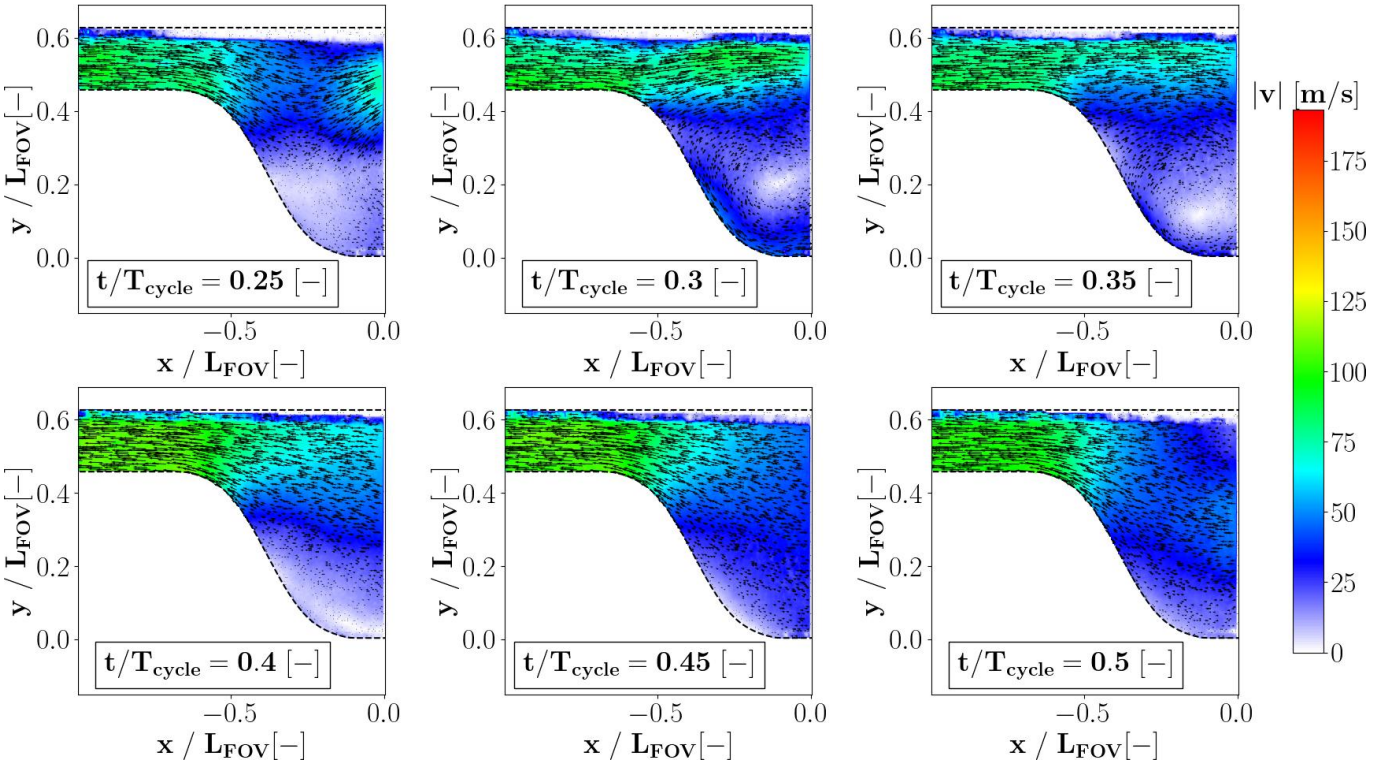


Figure 4: Velocity Field of Transition Duct at 25 %, 30 %, 35 %, 40 %, 45 % & 50 % of the cycle for Case *a*.

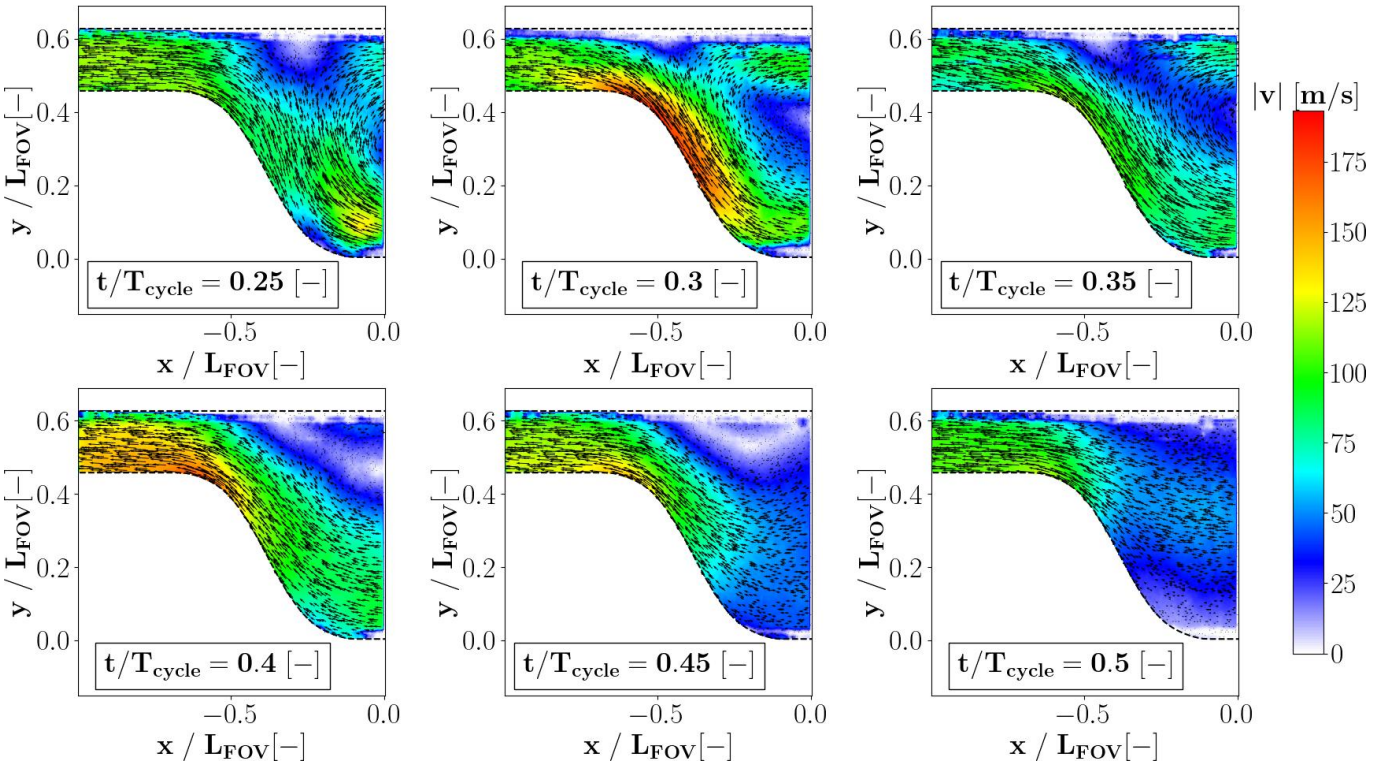


Figure 5: Velocity Field of Transition Duct at 25 %, 30 %, 35 %, 40 %, 45 % & 50 % of the cycle for Case *b*.

Similar remarks can be found for the case *b* (Fig. 7). The more accelerated flow field increases the maximum cycle average uncertainty levels, while oil deposition at the start of lower end-wall ($x/L_{FOV} \in [-0.154, 0]$, $y/L_{FOV} \in [0, 0.05]$) results in null values of uncertainty. In reality, the uncertainty at this location is quite high, since cross-correlation is unable to take place, as it is indicated at the velocity fields of Fig. 5. The PIV analysis cannot provide velocity vectors in this zone. Hence, the variation of the velocity vectors at this location is very low through time. Following Equations 4-8, the uncertainty of a

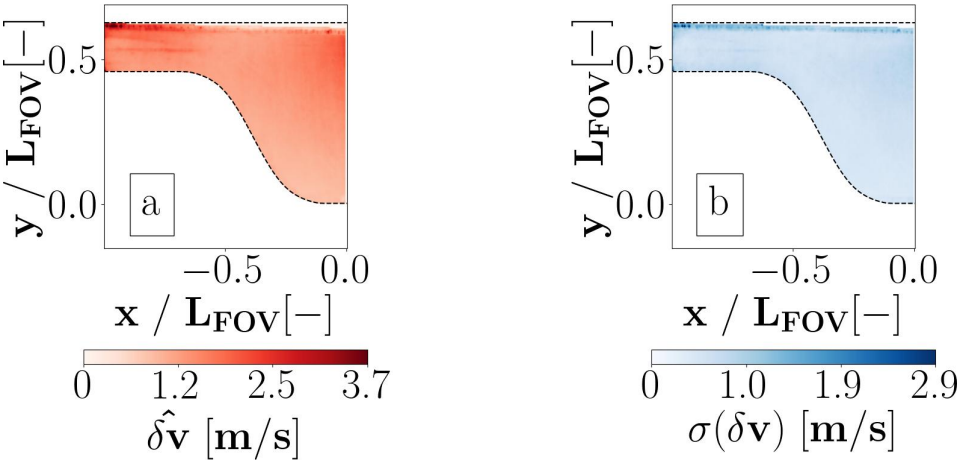


Figure 6: Cycle Average (a) and Standard Deviation (b) of Uncertainty Velocity Vector Profile for Case *a*.

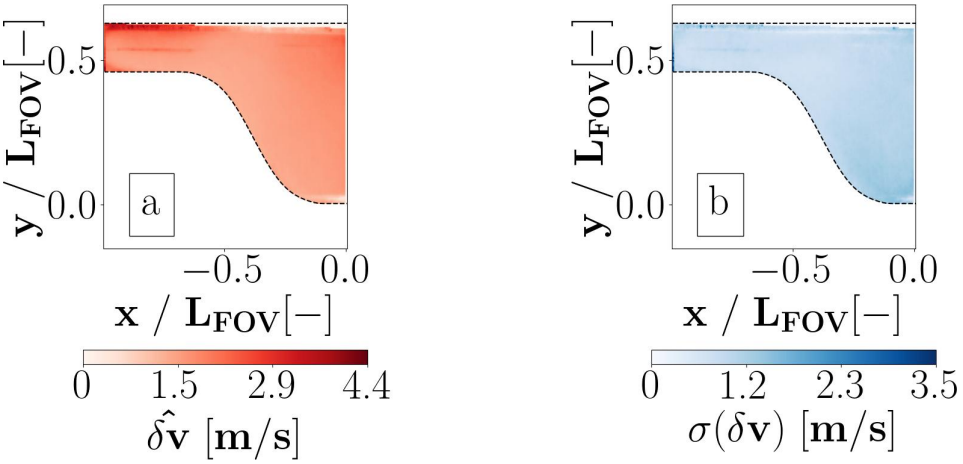


Figure 7: Cycle Average (a) and Standard Deviation (b) of Uncertainty Velocity Vector Profile for Case *b*.

correlation window that provides constantly low level of velocity will provide low level of uncertainty. At Table 3, the spatial average of cycle average and standard deviation of uncertainty velocity vector of the flow field for the two cases is presented. In general, the velocity field is characterized by low cycle average uncertainty for both cases, that in average does not exceed the 1 m/s.

Case	$\overline{(\hat{\delta}\mathbf{v})}$	$\sigma(\delta\mathbf{v})$
a	0.53 m/s	0.246 m/s
b	0.628 m/s	0.371 m/s

Table 3: Spatial Averaged Uncertainty Levels of Fig. 6 and 7.

3.3 Performance Evaluation

To evaluate the effectiveness of the transition duct in weakening the undesired fluctuations from the CVC, the PIV sample for the 25 % of cycle for case *b* is portrayed in Fig. 8 as an example. The inlet and outlet non-dimensional velocity profiles are illustrated in Fig. 8a, while the sample of PIV is placed in Fig. 8b. The sudden change of sign for the inlet velocity profile at $\frac{y_i}{dy_i} \approx 0.5$ can be observed. This change is justified by the vortex standing in the inlet of FOV. On the other hand, the outlet velocity profile is quite uniform. A metric to define the uniformity of the inlet and outlet velocity profile is the coefficient of variance ($COV_{x_i,y}$). The mean local velocity (Eq. 13) at a specific axial location x_i (inlet or outlet) is compared with the standard deviation of the vertical distribution ($y-$direction) of the velocity for the same axial location. This metric is given in Equation 14 and represents a useful property to quantify the deformation of the velocity with respect to the average value for a specific axial location.

$$\overline{u} = \frac{1}{y_{max} - y_{min}} \int_{y_{min}}^{y_{max}} u(x_i, y)\, dy \tag{13}$$

$$COV_{x_i,y} = \frac{\sigma[u(x_i,y)]}{\overline{u}} \tag{14}$$

Moreover, the turbulence level for the inlet and outlet of the transition duct can be specified. For that purpose, the turbulence kinetic energy (TKE) is normalized in accordance with the spatial average inlet velocity, as indicated in Equation 15. The temporal variation of spatial average inlet velocity of Equation 13 is used for this purpose. This property indicates how much turbulent is the inlet and outlet of the transition duct with respect the spatial average inlet veloc-

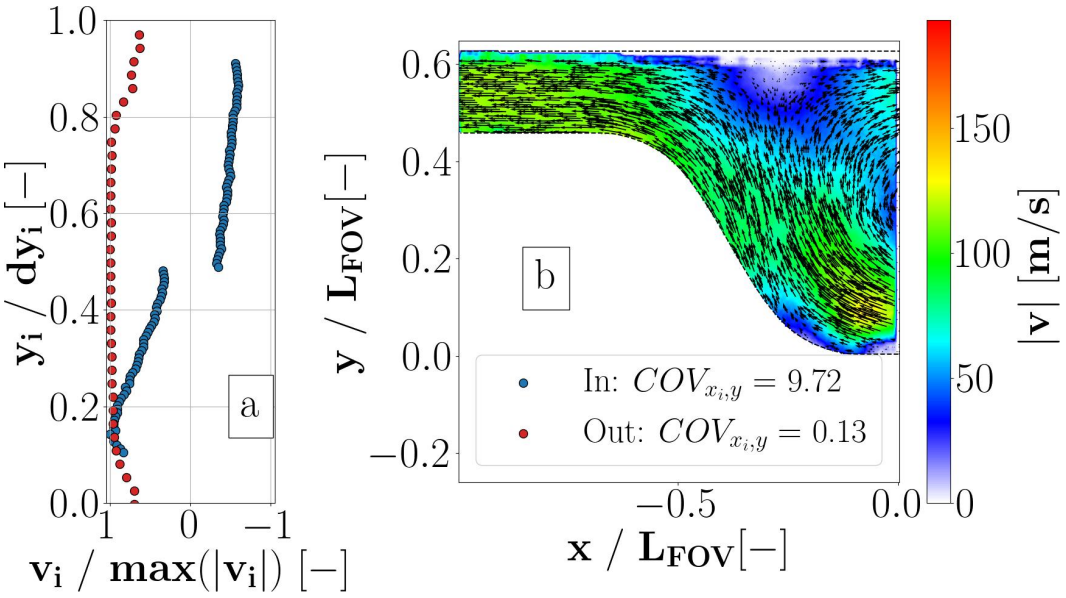


Figure 8: Distribution of Non-Dimensional Velocity at Inlet and Outlet of Transition Duct (a) and Velocity Flow Field at 25 % of cycle for Case *b* (b).

ity. The results of this analysis are shown in Table 4. For the 25 % of cycle instant currently shown, the outlet of transition duct achieves to drop the $COV_{x_i,y}$ by one order of magnitude, from 9.72 at the the inlet of the duct to 0.13. In conclusion, the transition duct accelerates the flow and generates a mostly uniform velocity profile for this specific instant.

$$\tilde{k} = \frac{TKE}{\frac{1}{2}\overline{u}_{in}^2} \tag{15}$$

Location	$\overline{\mathbf{u}}$	$\mathbf{COV_{x_i,y}}$	$\tilde{\mathbf{k}}$
Inlet	7.45 m/s	9.72	74.31
Outlet	106.36 m/s	0.13	30.35

Table 4: Performance Evaluation of the Transition Duct for 25% of Cycle for Case *b* in correspondence to Fig. 8.

This analysis can be extended to all the PIV samples. In Fig. 9, the spatially-averaged velocity, static pressure, $COV_{x_i,y}$ and $\tilde{k}$ for the case *a* are presented. In Fig. 9a, the average inlet and outlet velocity of the transition duct are inserted. In parallel, the pressure distribution of the inlet and outlet pressure sensor of the transition duct are included. In Fig. 9b, the $COV_{x_i,y}$ at inlet and outlet is reported. The same graphs are reported for the case *b* in Fig. 10. It can be observed that by increasing the inlet total pressure, the average outlet velocity level is increased. For the case *a* the $COV_{x_i,y}$ of inlet does not extremely differ by the one of outlet. On the contrary, a significant difference is observed between the inlet and outlet $COV_{x_i,y}$ for the case *b*, especially in the first time instants. As illustrated by the results of the PIV analysis, the increase of the inlet total pressure causes the flow field inside of the transition duct to accelerate further. It is interesting to notice that for the case *b* at every moment the outlet $COV_{x_i,y}$ is lower than the inlet. This means that the transition duct subtracts the velocity spatial non-uniformities at every instant. For the case *a* similar results are found.

Similarly with the velocity analysis (Fig. 9a and Fig. 10a) and $COV_{x_i,y}$ analysis (Fig. 9b and Fig. 10b) for the two cases, the study can be extended to the PLA evolution of turbulence in Fig. 9c and Fig. 10c. For both cases, turbulence level rises when the exhaust valves are open. Nonetheless, when the exhaust valves close, the turbulence level is relatively low for both inlet and outlet of the transition duct. Similar to the results of $COV_{x_i,y}$, the further reduced test rig pressure ratio of case *b* increases the turbulence level even more comparing to case *a* when the exhaust valves are open. This remark is also in accordance with the more intense presence of the clockwise rotating vortex at the inlet of the transition duct, as illustrated in Fig. 5.

After specifying the effect of the transition duct in the spatial resolution of the oscillations in the flow field, the time-dependent analysis is followed. For this purposes, the time-dependent coefficient of variation of the spatially-averaged (COV_t) inlet and outlet velocity profiles are calculated by Equation 16. In addition, the damping coefficient (D_{R_v}) of the transient spatially-averaged inlet and outlet velocity profiles is computed following Equation 17. The inlet and outlet COV_t illustrates what is the unsteadiness in time for these two locations. In addition, the damping coefficient of Equation 17 uncovers how much this temporal unsteadiness is attenuated or excited trough the transition duct.

$$COV_t = \frac{\sigma(\overline{u})}{\frac{1}{T}\int_0^T \overline{u}\, dt} \tag{16}$$

$$\hat{R_v} = \frac{Range(\overline{u})}{\frac{1}{T}\int_0^T \overline{u}\, dt} \rightarrow D_{\hat{R_v}} = \frac{\hat{R}_{v,\,In} - \hat{R}_{v,\,Out}}{\hat{R}_{v,\,Out}} \tag{17}$$

In Table 5, the results of the aforementioned analysis are presented. For both the cases, the outlet of the transition duct is characterized by a lower COV_t value. In fact, for both the

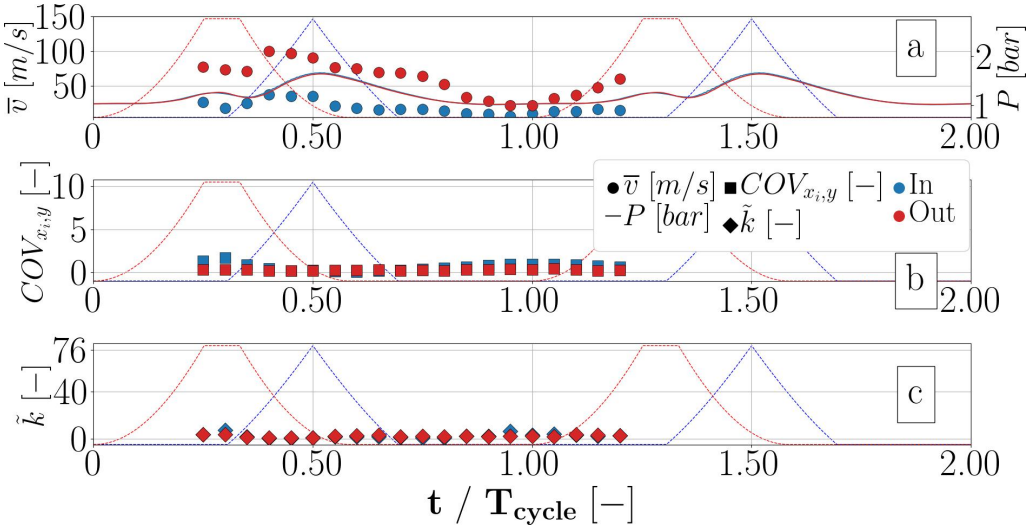


Figure 9: Evolution of Spatial Average Velocity, Static Pressure, $COV_{x_i,y}$ and $\tilde{k}$ for Case *a*.

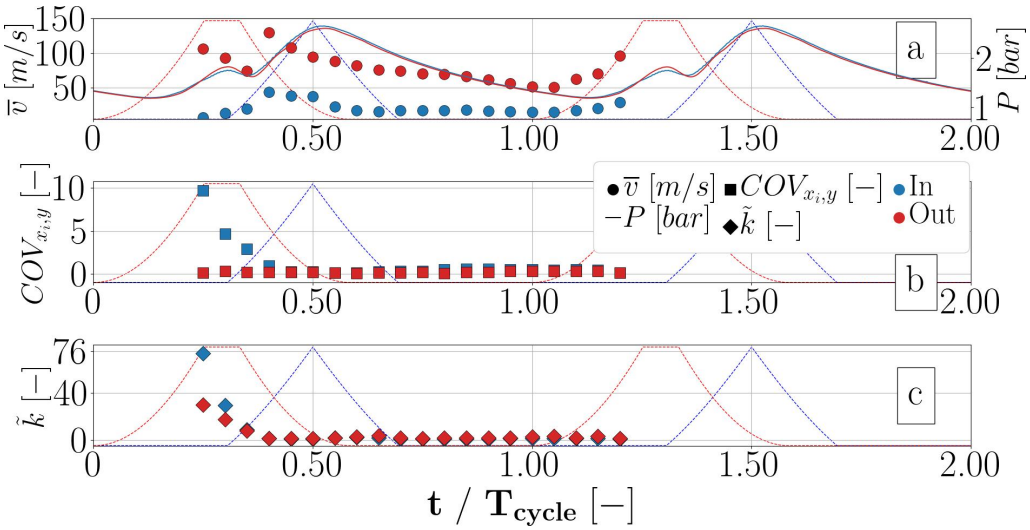


Figure 10: Evolution of Spatial Average Velocity, Static Pressure, $COV_{x_i,y}$ and $\tilde{k}$ for Case *b*.

Case	$COV_{t,\ inlet}$	$COV_{t,\ outlet}$	D_{R_v}
a	46.1 %	39.6 %	20.1 %
b	43.4 %	25.3 %	43.4 %

Table 5: Performance Evaluation of the Transition Duct.

cases the damping factor is positive. This means that the velocity fluctuation is attenuated in time. By comparing the two cases, it can be deduced that the COV_t of velocity for the inlet section is almost at the same level. Nevertheless, the transition duct is able to reach a lower COV_t for the case *b*. In fact, the attenuation of the temporal variation of the velocity is more than doubled when test rig pressure ratio decreases. In conclusion, the reduction of test rig pressure ratio greatly increases the $COV_{x_i,y}$ at the inlet, but low steady levels are achieved at the outlet (Fig. 9b and Fig. 10b). In parallel, the outlet COV_t is decreased, and a double attenuation of the temporal velocity perturbation is observed. Thus, the transition duct performance is superior for the case *b*. The reason for the better performance for the latter case is that the design of the transition duct was numerically conducted for a reactive case, in which the pressure ratio was closer to case *b* [31]. In conclusion, the transition duct achieves to successfully subtract the space-time variation of the velocity coming from the CVC at the two investigated test rig pressure ratios, at least in non-reactive conditions.

4 Conclusions

In the present study, the results of a non-reactive experimental campaign of a newly manufactured CVC exhaust system are described for test rig pressure ratios of 0.51 (*a*) and 0.25 (*b*). Even though neither injection nor ignition take place, the inlet and outlet rotary valves are set to an effective cycle frequency of 25 *Hz*, thus allowing the CVC chamber to experience a realistic filling-emptying process. As a result, a pulsating mass-flow of air is periodically expanded through the new exhaust system, which consists of a rectangular plenum, a transition

duct, a change area duct, and a circular converging-diverging nozzle. The instrumentation of the campaign includes fast response pressure probes and low-frequency PIV.

The static pressure measurements taken both upstream and downstream of the transition duct exhibit similar behavior for the two different test rig pressure ratios. For the high test rig pressure ratio, the transition duct only discharges the leakage flow by the exhaust valves when they are closed. Thus, it can approach the atmospheric pressure, while the nozzle remains fully subsonic. On the contrary, during the low pressure ratio tests the transition duct cannot reach the atmospheric pressure and the nozzle is choked for the 34 % of the cycle. The PIV results uncovered the presence of a vortex at the inlet of the transition duct for the moments when the exhaust valves are wide open. For the case of high pressure ratio, the rotation of the vortex is counterclockwise, whereas clockwise rotation is observed for the case of low pressure ratio. Nevertheless, the newly designed exhaust system is able to provide outflow without any spatial velocity deformation.

In conclusion, the newly manufactured transition duct can reach up to 20 % of attenuation of the transient spatial average velocity for the case *a*, and 43 % for the case *b*. In parallel, for the overwhelming majority of the time moments for both pressure ratios, the transition duct provides outflow with less coefficient of variance of local velocity distribution profile. As a consequence, the newly designed component alleviates the space-time fluctuation of the velocity flow field for two different conditions. Hence, if the transition duct connects the CVC to a subsequent HPT vane, the flow at the inlet of the stage would have significantly less velocity unsteadiness compared to the CVC exhaust. These findings are also relevant for the upcoming experimental analysis of the exhaust system in reactive conditions by the CVC using PIV.

Acknowledgments

The present activity is funded by the European Commission through the Marie Sklodowska-Curie action INSPIRE (Grant Agreement no. 956803). The authors would like to deeply thank Alain Claverie for his support and contribution in the experimental campaign.

Nomenclature

Roman letters

δv	Uncertainty of Velocity Vector $[m/s]$
$\hat{\delta v}$	Cycle Average Uncertainty of Velocity Vector $[m/s]$
Δt_l	Laser Pulse Separation Time $[s]$
A	Area $[m^2]$
$COV_{x_i,y}$	Spatial Coefficient of Variance of Velocity $[-]$
COV_t	Temporal Coefficient of Variance of Spatial Average Velocity $[-]$
$D_{\hat{R}_v}$	Damping Factor $[-]$
$\tilde{k}$	Non-Dimensional Turbulent Kinetic Energy $[-]$
L_T	Transition Duct Length $[m]$
P_t	Total Pressure $[Pa]$
P	Static Pressure $[Pa]$
$\hat{R}_v$	Reduced Range of Spatial Average Velocity $[-]$
$\tilde{v}$	Ensemble Average Velocity $[m/s]$
u, v	Velocity $[m/s]$
$\overline{u}$, $\overline{v}$	Spatial Average Velocity $[m/s]$
R	Specific Gas Constant $[J \cdot kg^{-1} \cdot K^{-1}]$
Re	Reynolds Number $[-]$
t	Time $[s]$
T	Period $[s]$
TKE	Turbulent Kinetic Energy $[m^2 \cdot s^{-2}]$

Greek letters

γ	Specific Heat Capacity Ratio $[-]$
π	Pressure Ratio $[-]$
μ	Dynamic Viscosity $[kg \cdot m^{-1} \cdot s^{-1}]$

Superscripts

$\hat{}$	Reduced

Subscripts

ΔX	Particle Displacement
Δt	Laser Pulse Separation
atm	Atmospheric
cr	Critical
$Char.$	Characteristic
M	Magnification
i	Location
In	Inlet
j	Grid Point
Out	Outlet
t	Total
T	Transition Duct
rig	Test Rig

Acronyms

CVC	Constant Volume Combustor
GT	Gas Turbines
HPT	High-Pressure Turbine
IGV	Inlet Guide Vanes
FOV	Field of View
Man.	Manufactured
Opt.	Optimized
PDE	Pulse Detonation Engine
PGC	Pressure Gain Combustors
PIV	Particle Image Velocimetry
PLA	Phase Locked-Averaging
RDE	Rotating Detonation Engine

References

[1] H. Holzwarth. *Rotary Combustion Engine*. Patent. U.S. Patent 1 234 56, Nov. 1969.

[2] I. Glassman, R. A. Yetter, and N. G. Glumac. "Flame phenomena in premixed combustible gases". In: *Combustion*. 5th ed. Waltham: Academic Press, 2015. Chap. 4, pp. 147–254. DOI: 10.1016/b978-0-12-407913-7.00004-9.

[3] W. H. Heiser and D. T. Pratt. "Thermodynamic Cycle Analysis of Pulse Detonation Engines". en. In: *Journal of Propulsion and Power* 18.1 (Jan. 2002), pp. 68–76. ISSN: 0748-4658, 1533-3876. DOI: 10.2514/2.5899.

[4] J. Z. Ma, M.-Y. Luan, Z.-J. Xia, J.-P. Wang, S.-j. Zhang, S.-b. Yao, and B. Wang. "Recent Progress, Development Trends, and Consideration of Continuous Detonation Engines". en. In: *AIAA Journal* 58.12 (Dec. 2020), pp. 4976–5035. ISSN: 0001-1452, 1533-385X. DOI: 10.2514/1.J058157.

[5] S. Salvadori, M. Insinna, and F. Martelli. "Unsteady Flows and Component Interaction in Turbomachinery". In: *International Journal of Turbomachinery, Propulsion and Power* 9.2 (2024), p. 15. DOI: 10.3390/ijtpp9020015.

[6] M. Fernelius, S. E. Gorrell, J. Hoke, and F. Schauer. "Effect of Periodic Pressure Pulses on Axial Turbine Performance". en. In: *49th AIAA/ASME/SAE/ASEE Joint Propulsion Conference*. San Jose, CA: AIAA, July 2013, p. 3687. ISBN: 9781624102226. DOI: 10.2514/6.2013-3687.

[7] M. H. Fernelius and S. E. Gorrell. "Mapping Efficiency of a Pulsing Flow-Driven Turbine". In: *Journal of Fluids Engineering* 142.6 (Mar. 2020), p. 061202. DOI: 10.1115/1.4045993.

[8] M. H. Fernelius and S. E. Gorrell. "Design of a Pulsing Flow Driven Turbine". en. In: *Journal of Fluids Engineering* 143.4 (Apr. 2021), p. 041501. ISSN: 0098-2202, 1528-901X. DOI: 10.1115/1.4049114.

[9] G. Roy, S. Frolov, A. Borisov, and D. Netzer. "Pulse detonation propulsion: challenges, current status, and future perspective". en. In: *Progress in Energy and Combustion Science* 30.6 (Jan. 2004), pp. 545–672. ISSN: 03601285. DOI: 10.1016/j.pecs.2004.05.001.

[10] M. Hishida, T. Fujiwara, and P. Wolanski. "Fundamentals of rotating detonations". en. In: *Shock Waves* 19.1 (Apr. 2009), pp. 1–10. ISSN: 0938-1287, 1432-2153. DOI: 10.1007/s00193-008-0178-2.

[11] F. K. Lu and E. M. Braun. "Rotating Detonation Wave Propulsion: Experimental Challenges, Modeling, and Engine Concepts". en. In: *Journal of Propulsion and Power* 30.5 (Sept. 2014), pp. 1125–1142. ISSN: 0748-4658, 1533-3876. DOI: 10.2514/1.B34802.

[12] G. Paniagua, M. Iorio, N. Vinha, and J. Sousa. "Design and analysis of pioneering high supersonic axial turbines". en. In: *International Journal of Mechanical Sciences* 89 (Dec. 2014), pp. 65–77. ISSN: 00207403. DOI: 10.1016/j.ijmecsci.2014.08.014.

[13] Z. Liu, J. Braun, and G. Paniagua. "Performance of axial turbines exposed to large fluctuations". en. In: *53rd AIAA/SAE/ASEE Joint Propulsion Conference*. Atlanta, GA: AIAA, July 2017, p. 4817. ISBN: 9781624105111. DOI: 10.2514/6.2017-4817.

[14] Z. Liu, J. Braun, and G. Paniagua. "Integration of a transonic high-pressure turbine with a rotating detonation combustor and a diffuser". en. In: *International Journal of Turbo and Jet-Engines* 40.1 (Mar. 2023), pp. 1–10. ISSN: 0334-0082, 2191-0332. DOI: 10.1515/tjj-2020-0016.

[15] Z. Liu, J. Braun, and G. Paniagua. "Thermal power plant upgrade via a rotating detonation combustor and retrofitted turbine with optimized endwalls". en. In: *International Journal of Mechanical Sciences* 188 (Dec. 2020), p. 105918. ISSN: 00207403. DOI: 10.1016/j.ijmecsci.2020.105918.

[16] S. Grasa and G. Paniagua. "Design, Multi-Point Optimization and Analysis of Diffusive Stator Vanes to Enable Turbine Integration Into Rotating Detonation Engines". In: *Turbo Expo: Power for Land, Sea, and Air*. Vol. 86984. American Society of Mechanical Engineers. 2023, V005T06A007. DOI: https://doi.org/10.1115/GT2023-101726.

[17] S. Grasa and G. Paniagua. "Design and Characterization of Highly Diffusive Turbine Vanes Suitable for Transonic Rotating Detonation Combustors". In: *International Journal of Turbomachinery, Propulsion and Power* 9.2 (May 2024), p. 18. ISSN: 2504-186X. DOI: 10.3390/ijtpp9020018.

[18] P. Gallis, S. Salvadori, and D. A. Misul. "Numerical Analysis of a Flow Control System for High-Pressure Turbine Vanes Subject to Highly Oscillating Inflow Conditions". In: *Turbo Expo: Power for Land, Sea, and Air*. Vol. 87974. American Society of Mechanical Engineers. 2024, V005T06A021. DOI: 10.1115/gt2024-126791.

[19] A. Naples, J. Hoke, R. Battelle, and F. Schauer. "T63 Turbine Response to Rotating Detonation Combustor Exhaust Flow". en. In: *Journal of Engineering for Gas Turbines and Power* 141.2 (Feb. 2019), p. 021029. ISSN: 0742-4795, 1528-8919. DOI: 10.1115/1.4041135.

[20] S. Zhou, H. Ma, S. Li, D. Liu, Y. Yan, and C. Zhou. "Effects of a turbine guide vane on hydrogen-air rotating detonation wave propagation characteristics". In: *International Journal of Hydrogen Energy* 42.31 (Aug. 2017), pp. 20297–20305. ISSN: 0360-3199. DOI: 10.1016/j.ijhydene.2017.06.115.

[21] W.-l. Wei, Y.-w. Wu, C.-s. Weng, and Q. Zheng. "Influence of propagation direction on operation performance of rotating detonation combustor with turbine guide vane". In: *Defence Technology* 17.5 (Oct. 2021), pp. 1617–1624. ISSN: 2214-9147. DOI: 10.1016/j.dt.2020.08.009.

[22] Y. Wu, C. Weng, Q. Zheng, W. Wei, and Q. Bai. "Experimental research on the performance of a rotating detonation combustor with a turbine guide vane". In: *Energy* 218 (Mar. 2021), p. 119580. ISSN: 0360-5442. DOI: 10.1016/j.energy.2020.119580.

[23] E. Bach, C. O. Paschereit, P. Stathopoulos, and M. D. Bohon. "Rotating Detonation Wave Direction and the Influence of Nozzle Guide Vane Inclination". In: *AIAA Journal* 59.12 (Dec. 2021), pp. 5276–5287. ISSN: 1533-385X. DOI: 10.2514/1.j060594.

[24] A. Glaser, N. Caldwell, and E. Gutmark. "Performance Measurements of a Pulse Detonation Combustor Array Integrated with an Axial Flow Turbine". In: *44th AIAA Aerospace Sciences Meeting and Exhibit*. American Institute of Aeronautics and Astronautics, Jan. 2006. DOI: 10.2514/6.2006-1232.

[25] B. Boust, Q. Michalski, and M. Bellenoue. "Experimental Investigation of Ignition and Combustion Processes in a Constant-Volume Combustion Chamber for Air-Breathing Propulsion". en. In: *52nd AIAA/SAE/ASEE Joint Propulsion Conference*. Salt Lake City, UT: AIAA, July 2016, p. 4699. ISBN: 9781624104060. DOI: 10.2514/6.2016-4699.

[26] B. Boust, M. Bellenoue, and Q. Michalski. "Pressure gain and specific impulse measurements in a constant-volume combustor coupled to an exhaust plenum". In: *Active Flow and Combustion Control 2021*. Berlin, Germany: Springer, 2022, pp. 3–15. DOI: 10.1007/978-3-030-90727-3_1.

[27] L. Labarrere, T. Poinsot, A. Dauptain, F. Duchaine, M. Bellenoue, and B. Boust. "Experimental and numerical study of cyclic variations in a Constant Volume Combustion chamber". en. In: *Combustion and Flame* 172 (Oct. 2016), pp. 49–61. ISSN: 00102180. DOI: 10.1016/j.combustflame.2016.06.027.

[28] P. Gallis, D. A. Misul, S. Salvadori, M. Bellenoue, and B. Boust. "Development and Validation of a 0-D/1-D Model to Evaluate Pulsating Conditions from a Constant Volume Combustor". In: *Joint Meeting of International Workshop on Detonation for Propulsion (IWDP) and International Constant Volume and Detonation Combustion Workshop (ICVDCW)*. Berlin, Germany, Aug. 2022. DOI: 10.5281/zenodo.7137725.

[29] P. Gallis, D. A. Misul, M. Bellenoue, B. Boust, and S. Salvadori. "Development of 1D Model of Constant-Volume Combustor and Numerical Analysis of the Exhaust Nozzle". In: *Energies* 17.5 (2024), p. 1191. DOI: https://doi.org/10.3390/en17051191.

[30] P. Gallis, D. Misul, B. Boust, M. Bellenoue, S. Salvadori, et al. "Experimental Inert Characterization of an Exhaust System Downstream of a CVC". In: *Proceedings of the 13th International Workshop on Detonation for Propulsion (IWDP 2024)*. Ann Arbor, USA, July 2024.

[31] P. Gallis, D. Misul, B. Boust, M. Bellenoue, and S. Salvadori. "Numerical Analysis and Design of New Exhaust Section Downstream of Constant Volume Combustor". In: *Journal of Engineering for Gas Turbines and Power* (Aug. 2024), pp. 1–43. ISSN: 0742-4795. DOI: 10.1115/1.4066253. eprint: https://asmedigitalcollection.asme.org/gasturbinespower/article-pdf/doi/10.1115/1.4066253/7363859/gtp-24-1417.pdf.

[32] T. Arts, M. Lambert de Rouvroit, and A. W. Rutherford. *Aero-thermal investigation of a highly-loaded transonic linear turbine guide vane cascade*. Tech. rep. von Karman Institute for Fluid Dynamics, 1990.

[33] International Organization for Standardization. *Measurement of Gas Flow by Means of Critical Flow Venturi Nozzles*. DS/EN ISO 9300; Dansk Standard. American National Standards Institute: New York, NY, USA. 1987.

[34] L. GmbH. *Manual n^o 1003001 for DaVis Software*. Anna Vandenhoeck- ring 19/ D-37081, Göttingen, Germany, Nov. 2024.

[35] A. Sciacchitano. "Uncertainty quantification in particle image velocimetry". In: *Measurement Science and Technology* 30.9 (July 2019), p. 092001. ISSN: 1361-6501. DOI: 10.1088/1361-6501/ab1db8.